State-to-State Differential Cross Sections by Velocity Mapping for Rotational Excitation of CO by Ne

K. Thomas Lorenz[†] **and David W. Chandler**

Combustion Research Facility, Sandia National Laboratory, Livermore, California 94550

George C. McBane*[,‡]

Department of Chemistry, The Ohio State University, Columbus, Ohio 43210

Received: September 10, 2001; In Final Form: November 30, 2001

State-to-state differential cross sections for rotational excitation of CO by Ne were determined in a crossed beam experiment at 511 cm^{-1}. Scattered CO molecules were ionized with 2+1 resonance enhanced multiphoton ionization and detected with velocity mapping. Cross sections were determined for most of the energetically allowed final states of CO. The results were compared with predictions from two Ne−CO ab initio potential surfaces. The CCSD(T) surface of McBane and Cybulski [*J. Chem. Phys*. **1999**, *110*, 11734] predicts the positions of the rotational rainbow maxima more accurately than does the surface of Moszynski et al. [*J. Phys. Chem. A* **1997**, *101*, 4690].

1. Introduction

Interactions between neon and carbon monoxide have no particular practical importance, but they provide an excellent test case for high-precision calculations of intermolecular forces. All three atoms are heavy (in the quantum-chemical sense: "more than two electrons") but not so large that good electronic structure calculations are prohibitively difficult. Two high quality potential surfaces with analytic fits are available. The first, by Moszynski et al.,[1] was developed with symmetry adapted perturbation theory[2] (SAPT). A later surface ("S2") by McBane and Cybulski used the supermolecule approach at the CCSD-(T) level.[3] Subramanian et al. reported supermolecule ab initio interaction energies calculated with the MP4 method and a smaller basis set than that used by McBane and Cybulski, but they did not report an analytic fit.[4]

A good experimental data set is needed for comparison with the theoretical predictions. Transport,[5−7] virial,[8−10] and pressure broadening[11,12] data are available. McKellar and co-workers have recorded and analyzed NeCO infrared spectra, including a few hot bands, on the CO stretching fundamental.[13,14] Pure rotational spectra have also been reported: Walker et al. reported nine *a*-type (end-over-end tumbling) microwave transitions,[15] and Winnewisser et al. reported seven *b*-type (CO rotational excitation) millimeter wave lines.[16] Antonova et al.[17] measured relative state-to-state integral cross sections for rotational excitation of CO in collisions with Ne at collision energies near 700 and 800 cm^{-1}.

McBane and Cybulski tested the SAPT and CCSD(T) potentials against spectroscopic, virial, pressure broadening, and integral cross section data.[3] They concluded that the SAPT surface gave a better description of the van der Waals well, that the well on the SAPT surface was a little too deep, whereas that on the CCSD(T) surface was a little too shallow, and that there was modest evidence that the CCSD(T) surface gave a better description of the repulsive wall. They showed that state-to-state differential cross sections for Ne−CO scattering would be able to provide clear discrimination between the two candidates. The present paper reports experimental measurements of those cross sections and comparisons with the two surfaces.

The measurements were performed with a crossed supersonic beam apparatus. CO molecules scattered into particular final states were photoionized in the beam crossing region, and their angular distribution was determined with velocity mapping.[18] This approach provides good angular resolution, perfect final *j* selection, and a very large efficiency advantage over movable-detector methods.[19] Early applications of ion imaging to crossed beam experiments include studies of Ar−NO scattering[20] and $H + H_2$ reactions.[21] Several more examples have appeared recently.[22−27]

2. Experiment

The data were collected in a crossed molecular beam machine with REMPI ionization of the scattered products and velocity mapping detection. The apparatus has been fully described elsewhere.[26]

Two supersonic beams, one of neat Ne and the other of 5% CO seeded in Ar, were produced by pulsed piezoelectric valves of the Proch and Trickl design.[28] Both beams passed through skimmers (Beam Dynamics; 0.6 mm orifice, 27 mm from valves) and collimators (0.82 mm orifice, 76 mm from skimmer orifices) before intersecting in the scattering chamber 29 mm beyond the collimators. The valves, skimmers, and collimators were all mounted on a single carefully machined support so that their alignment was assured. All five vacuum chambers (two source chambers, two intermediate chambers between skimmers and collimators, and the scattering chamber) were

* To whom correspondence should be addressed. E-mail: mcbaneg@gvsu.edu.

[†] Current address: Lawrence Livermore National Laboratory, Livermore, CA 94550.

[‡] Current address: Department of Chemistry, Grand Valley State University, Allendale, MI 49401.

10.1021/jp013441t CCC: $22.00
Published on Web 01/29/2002

evacuated by turbomolecular pumps. Stagnation pressures for the expansions were 1.5 bar for the CO/Ar mixture and 2.5 bar for the Ne.

Scattered CO molecules were probed by 2+1 resonance enhanced multiphoton ionization on the $E\ ^1\Pi \leftarrow X\ ^1\Sigma^+$ (0,0) transition.[29] All of the data were collected in the strong, well resolved *S* branch. A dye laser (Lambda Physik Scanmate) operating with Exalite 428 or Stilbene 3 dyes was pumped by a Coherent Infinity Nd:YAG laser. The laser frequency was fixed during each image collection. (The effect of the resulting Doppler selection of scattered molecules was accounted for in the data analysis described later.) The dye laser output was doubled in a BBO crystal to provide probe light near 215 nm. The probe beam was focused with a half-meter lens onto the intersection region of the molecular beams. The laser beam was in the same plane as the two molecular beams and bisected them, propagating toward the oncoming molecules. It was linearly polarized in the beam plane.

Velocity mapping ion optics extracted the ions from the intersection volume and accelerated them toward the detector. The optics included an asymmetric immersion lens such as that described by Eppink and Parker[18] and a standard Einzel lens. The detector was a 75 mm diameter pair of microchannel plates in front of a fast phosphor screen (Galileo). The voltage on the front microchannel plate was applied in a narrow pulse to provide mass discrimination. The ion image formed on the screen was detected by a CCD camera (Photometrics) with a standard camera lens. The laser and both molecular beams ran at 20 Hz. Signal and background images, 600 shots (30 s) each, were collected alternately; for the background images, the timing of the Ne beam was changed so that it did not overlap with the CO and laser beams. The difference between signal and background was accumulated over typically 30 min of laboratory time to form a single image for analysis.

To locate the spectral lines and determine the initial rotational populations of CO, the CCD camera was replaced with a photomultiplier. This arrangement permitted collection of ordinary REMPI spectra. The fractional population of CO in $j_i = 0$ was 77%, with nearly all of the rest in $j_i = 1$. These populations correspond to a rotational temperature of 2.4 K, though a small high-*j* "tail" corresponding to a much higher temperature was present in the rotational distribution.

3. Results

3.1. Raw Data and Qualitative Observations. The raw data images for $\Delta j = 3-14$ are shown in Figure 1. A reconstruction from the fitted DCS appears to the right of each raw image; these are described in later sections. Velocity mapping implies that the axes in these plots may be regarded as velocity components in the plane parallel to the detector face. Figure 2 shows the data for $j_f = 8$ with the corresponding Newton diagram overlaid. All of the images have the same orientation and scale. The color map for each pair is set so that the brightest pixel in the reconstructed image (which has no noise) is white.

In each image, a ring centered on the center of mass velocity is prominent. This extra brightness on the edge, as compared to the center, of the image is caused by "piling up" of molecules with different velocity components out of the plane of the image. The variation in intensity around the ring, from forward scattering (near the initial CO velocity) to backscattering (near the initial Ne velocity), contains information about the differential cross section.

Qualitative conclusions about structure in the differential cross section may be made directly from the images. Several of them show clear multiple maxima and minima; in general, these structures move to higher scattering angles as Δj increases. For $\Delta j \geq 10$, very little intensity appears at small scattering angles.

In most images, features near the top of the image appear brighter than corresponding features near the bottom. This asymmetry is a consequence of a density-to-flux transformation: molecules moving slowly in the laboratory, or moving along the propagation direction of the probe laser, could be scattered some time before the laser pulse and still be detected. Molecules moving more rapidly, especially perpendicular to the probe laser, escape detection quickly so only the ones scattered just before the probe pulse are detected. This velocity-dependent detection probability is the primary systematic effect that must be accounted for in quantitative extraction of differential cross sections from the data.

3.2. Collision Energy Calibration. In a velocity mapping experiment, each position on the two-dimensional detector corresponds to a particular velocity vector projection in the plane of the detector, and the mapping is linear. In the absence of calibration experiments, the proportionality constant is not known at the beginning of an experiment. In these inelastic scattering experiments, however, an internal calibration is available. The energy spacings between different rotational levels of CO are known. Images with different j_f show Newton spheres that have accurately known differences in the postcollision center of mass translational energies. Comparison of the measured diameters (in pixels) of the projected Newton spheres therefore provides an absolute determination of the speed-to-position velocity mapping factor and of the center of mass collision energy in the system. A useful working equation is

$$d = \frac{2}{m_{CO}}\left(\frac{2(E - \Delta E)}{\mu}\right)^{1/2} b \qquad (1)$$

where d is the measured diameter of the projected Newton sphere, E is the collision energy in the center of mass frame, ΔE is the energy transferred into rotation of CO, μ is the reduced mass of the Ne−CO system, and b is the speed-to-position mapping factor. A fit of eq 1 to the measured diameters of the Newton spheres gave the result $E = 511 \pm 15$ cm^{-1}, indicating an operating temperature for both valves near 333 K. Speed ratios estimated from sizes of unscattered beam spots indicate that the collision energy distribution has width $\sigma_E \approx 25$ cm^{-1}.

4. Analysis

In velocity mapped photodissociation, a direct inversion of the image data via an inverse Abel transform is useful.[30] In the current experiments, such a direct inversion is not available for two reasons. First, the cylindrical symmetry required by the Abel transform is not present; the intersection of the probe laser with the expanding spheres of scattered products does not possess cylindrical symmetry. Second, the distribution of speeds in the two molecular beams blurs the images in a nonuniform way. Therefore, we analyzed the images with a fitting method.

In the fitting procedure, a basis set of narrow, sharply peaked differential cross sections was first chosen on a uniformly spaced grid in scattering angle. A realistic simulation transformed each of these basis functions into the image space. The resulting set of basis images could then be used as a linear basis set for a direct χ^2 fit to the data image. The fitting coefficients gave the DCS values on the original grid directly. The remainder of this section describes the DCS basis, the simulation procedure, and the fitting procedure in more detail.

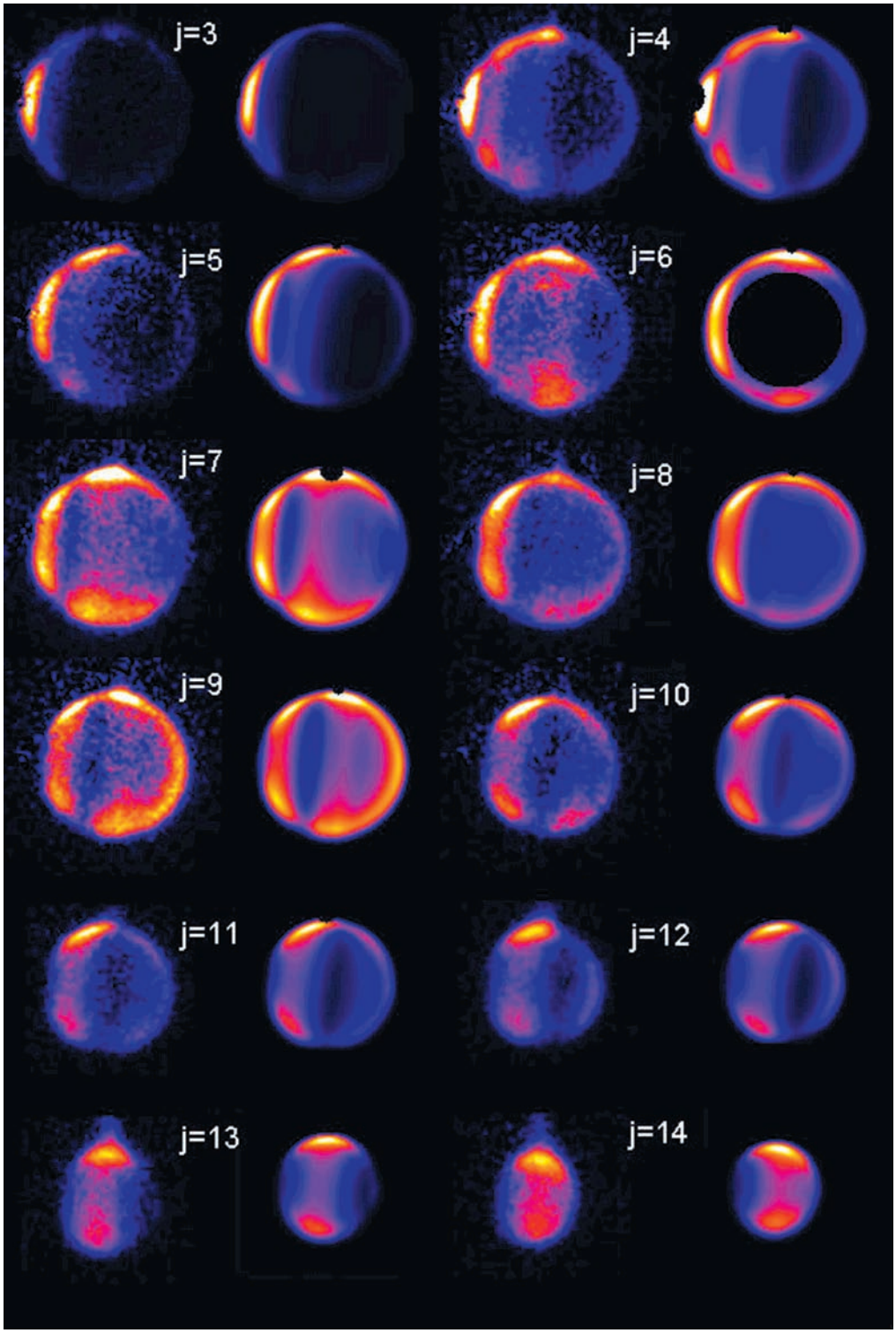

Figure 1. Raw data (left member of each pair) and simulated version reconstructed from fitted differential cross section (right member). Regions that appear black in the reconstructed images were excluded from the fitting procedure.

4.1. Basis Set. The state-to-state differential cross section for each rotational transition was modeled as a piecewise linear, continuous function on an evenly spaced 5° grid in scattering angle. Such a function may be written as a weighted sum of basis functions each of which is a triangle with value 1 at its peak, decreasing to value 0 at the peak positions of the basis functions on either side. The weighting coefficients are simply the values of the differential cross section at the grid points. This basis scheme is very similar to one used by Winterhalter et al. in their paper on photoelectron imaging.[31]

4.2. Image Simulation. The image simulation procedure takes as input a differential cross section $I(\theta)$ and a physical description of the experiment and provides as output a predicted image (intensity vs pixel position). The important characteristics of the experiment included in the simulation are the speed distributions, temporal profiles, and spatial extents of the two molecular beams; the probe laser beam intensity as a function of position and wavelength; the intensity dependence of the ionization process; the characteristics of the velocity mapping ion optics; and the position and orientation of the detector.

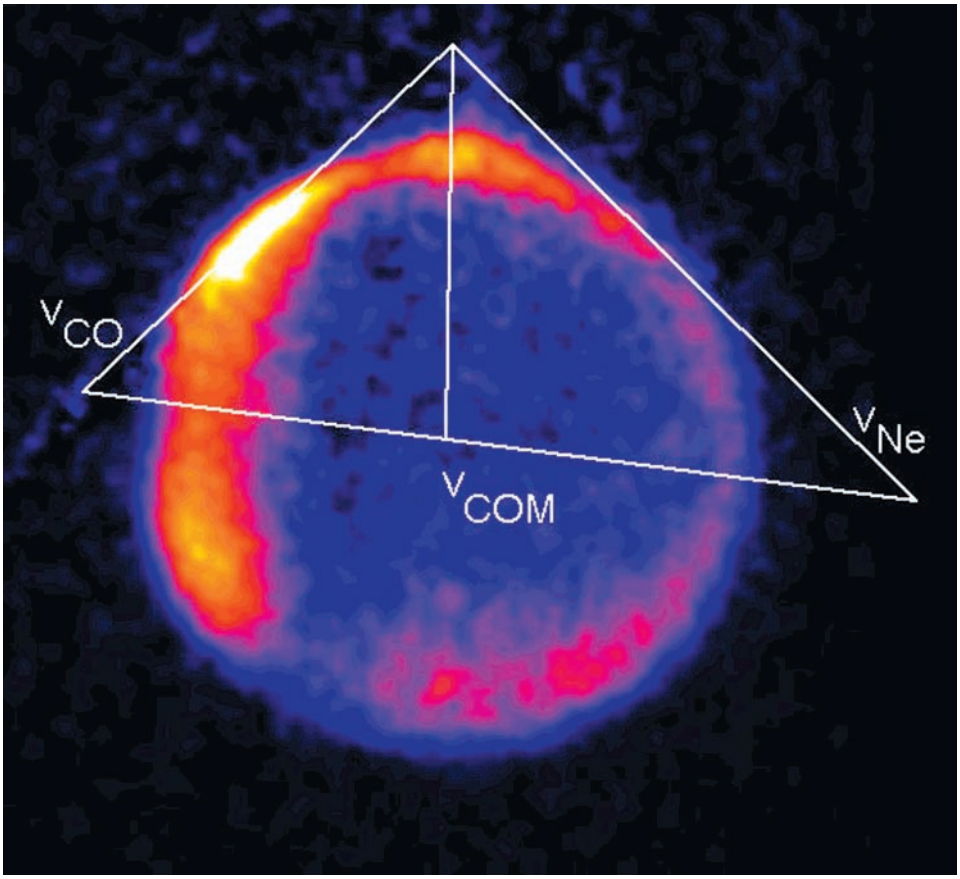

Figure 2. Raw data for $j_f = 8$ with corresponding Newton diagram. The intersection near the top of the image gives the laboratory frame origin.

A detailed description and derivation of the simulation procedure has been given elsewhere.[32] We begin with an assumption that the velocity mapping optics work perfectly for ions formed within a specific collection volume V_{coll} and completely reject any ions formed outside that volume. Then, each pixel on the detector corresponds to a definite small range of values of v_x and v_y for the ions.

Under the assumption of perfect velocity mapping, the intensity in a particular pixel is given by

$$I \propto \int\int d\mathbf{v}_A\, d\mathbf{v}_B\, g(\mathbf{v}_A) g(\mathbf{v}_B) g \int_{\text{pixel}}\int dv_x dv_y \int_{-\infty}^{0} dt \int_{V_{coll}}\int\int d\mathbf{r} \times \left[P_I(\mathbf{r},\mathbf{v}_+,\mathbf{j})\, n_A(\mathbf{r}+\mathbf{v}_+ t,\, t)\, n_B(\mathbf{r}+\mathbf{v}_+ t, t)\, \frac{d\sigma}{d\omega}(\mathbf{v}_+) J(\mathbf{v}_+) + P_I(\mathbf{r},\mathbf{v}_-,\mathbf{j}) n_A(\mathbf{r}+\mathbf{v}_- t, t) n_B(\mathbf{r}+\mathbf{v}_- t, t) \frac{d\sigma}{d\omega}(\mathbf{v}_-) J(\mathbf{v}_-) \right] \quad (2)$$

In eq 2, $\mathbf{v}_A$ and $\mathbf{v}_B$ are the precollision velocities of the colliding molecules and $g(\mathbf{v}_A)$ and $g(\mathbf{v}_B)$ are their distributions in the molecular beams. v_x and v_y are the components of the postcollision laboratory frame velocity of the scattered A molecule in the plane of the detector. The initial relative speed is $g = |\mathbf{v}_A - \mathbf{v}_B|$, and t is the difference between the times of the scattering event and the firing of the probe laser. $\mathbf{v}_+$ and $\mathbf{v}_-$ represent the two possible laboratory frame velocity vectors of the scattered molecule for particular $\mathbf{v}_A$, $\mathbf{v}_B$, v_x, and v_y; typically two positions on the Newton sphere will correspond to the same position on the detector. $P_I(\mathbf{r},\mathbf{v},\mathbf{j})$ is the ionization probability for an A molecule at position $\mathbf{r}$ with velocity $\mathbf{v}$ and angular momentum $\mathbf{j}$ when the probe laser fires. It depends on $\mathbf{r}$ through the spatial dependence of the laser intensity, on $\mathbf{v}$ through the Doppler shift, and on $\mathbf{j}$ through the orientation dependence of the ionization probability. $n_A(\mathbf{r},t)$ and $n_B(\mathbf{r},t)$ give the densities of A and B molecules in the molecular beams at position $\mathbf{r}$ and time t. They appear with shifted position arguments in the intensity expression, $n_A(\mathbf{r}+\mathbf{v}t,t)$, because molecules scattered at time t (which is negative) and position $\mathbf{r}+\mathbf{v}t$ will arrive at position $\mathbf{r}$ to be ionized at time $t = 0$. $J(\mathbf{v})$ gives the Jacobian for projection of the Newton sphere onto the planar detector; it is proportional to $(|\mathbf{v}\cdot\mathbf{e}_z|)^{-1}$, where $\mathbf{e}_z$ is a unit vector perpendicular to the detector face (that is, along the flight tube direction). The two terms $J(\mathbf{v}_+)$ and $J(\mathbf{v}_-)$ are equal. $d\sigma/d\omega(\mathbf{v})$ is the differential cross section.

Equation 2 is a twelve-dimensional integral. To simplify it, we make two further assumptions: that the angular divergence of each molecular beam is negligible and that the only term in eq 2 that varies rapidly within a single pixel is the Jacobian $J(\mathbf{v})$. In the experiments, the beams were very tightly collimated, with divergence half-angles less than 0.25°. Neglecting the angular divergence reduces the six-dimensional integral over $\mathbf{v}_A$ and $\mathbf{v}_B$ to a two-dimensional one over the speed distributions in the two beams. Regarding all of the functions of $\mathbf{v}$ except $J(\mathbf{v})$ as slowly varying over any single pixel permits the factorization

$$I \propto \int\int dv_A\, dv_B\, g(v_A)\, g(v_B) g[\int_{\text{pixel}}\int dv_x\, dv_y\, J(\mathbf{v}_+)] \times \int_{-\infty}^{0} dt \int_{V_{coll}}\int\int d\mathbf{r} \left[P_I(\mathbf{r},\bar{\mathbf{v}}_+,\mathbf{j})\, n_A(\mathbf{r}+\bar{\mathbf{v}}_+ t, t)\, n_B(\mathbf{r}+\bar{\mathbf{v}}_+ t, t) \times \frac{d\sigma}{d\omega}(\bar{\mathbf{v}}_+) + P_I(\mathbf{r},\bar{\mathbf{v}}_-,\mathbf{j})\, n_A(\mathbf{r}+\bar{\mathbf{v}}_- t, t)\, n_B(\mathbf{r}+\bar{\mathbf{v}}_- t, t) \frac{d\sigma}{d\omega}(\bar{\mathbf{v}}_-) \right] \quad (3)$$

where $\bar{\mathbf{v}}_+$ and $\bar{\mathbf{v}}_-$ represent the two possible laboratory frame

velocities for a molecule whose v_x and v_y are those corresponding to the center of the pixel.

The simulation program implements eq 3 for particular choices of g_A, g_B, n_A, n_B, and P_I. The velocity distribution functions g_A and g_B are assumed to be Gaussian, with speed ratios determined from unscattered spot sizes. The molecular beam intensity distribution is assumed to be a step function in the radial directions and Gaussian in time, and collimated along its axis. P_I is assumed to be a separable function of **r**, **v**, and **j**. The spatial part is the ordinary spatial distribution of a focused Gaussian beam, raised to the second power for this 2+1 REMPI probe. The velocity part is the square of a Gaussian wavelength spectrum evaluated at the Doppler-shifted absorption frequency of the molecule. For our geometry, with the laser beam propagating parallel to the face of the detector, the Doppler part of P_I is simply a function of pixel position and can be multiplied pixel by pixel into the image after the main part of the simulation has been completed. In most of the analysis presented here, the **j** dependence was ignored.

The two-dimensional integral of the Jacobian over the pixel position was performed analytically. The integrals over t and **r** were performed with nested Gaussian quadratures for a representative set of v_z at each pixel and then interpolated for other v_z. The integrals over the speed distributions in the two molecular beams were done with trapezoidal rule integration using 30 speeds in each molecular beam. In the final program, each image simulation (evaluation of eq 3 for every pixel) required about 5 min, with the run time dominated by evaluations of the analytic Jacobian integral.

4.3. Fitting Procedure. Each basis function in the differential cross section space was used as input to the simulation program; the corresponding output images formed a linearly independent, but not orthogonal, basis set in the image space. These basis functions could often be fit with singular value decomposition directly to the data image. However, that procedure occasionally produced unphysical results, particularly at low and high scattering angles where the basis functions in the image space have the greatest overlap. We therefore used a first-order regularization method.[33] In parts of the DCS space where the data constrain the DCS well, this approach respects that constraint. In regions where the data do not constrain the DCS effectively, the first order regularization tends to choose DCS values that are equal to the values at neighboring angles. It was fairly easy to choose an appropriate balance between minimization of χ^2 and preference for a constant differential cross section.

The data images do not have sharp edges at the limits of the Newton circle for two reasons: finite speed distributions in the molecular beams smooth the edges, and imperfections in the velocity mapping add an additional slight blurring. The effect of the speed distributions is accurately accounted for in the simulation. To reduce the effects of the ion optical blurring on the fitted parameters, each basis image was convolved with a narrow point spread function before the fitting procedure. The point spread function was chosen empirically to match the slopes of sharp features in simulated and observed images; a conical point spread function with a radius of 4 pixels at its base was appropriate for most images.

Some regions of the data images could not be used for the analysis. These regions appear as black disks in the reconstructed images in Figure 1. At low j_f, unscattered population in the molecular beam obscures the signal from scattered molecules near the initial CO velocity vector. In addition, there are small ion optical artifacts ("hot spots") near the tops of several images; these spots were excluded from the fitting and appear most clearly in the reconstructed images for $j_f = 4$ and 7. Finally, the $R(13)$ spectral line partially overlaps the $S(6)$ line, so that scattered $j_f = 13$ ions appear in the interior of the $j_f = 6$ image; that image was therefore analyzed using only the outer ring.

Each image was subjected to a "two-level" fitting procedure. An outer nonlinear fitting loop sought optimum values of the detector position and orientation, velocity mapping factor (effective flight time), and laser frequency offset from the center of the absorption line. At each iteration of the nonlinear optimization, new basis images were interpolated from the original simulated set, and then a regularized linear fit was performed as described above. Only the fitted laser frequency offset varied substantially from one image to the next, as expected. However, the fitted value of the frequency offset can be affected by slight misestimates of the other detection parameters, so the multiparameter optimization was important for good fits.

5. Results

5.1. Extracted Differential Cross Sections. Figure 3 displays the extracted differential cross sections for final rotational states with $3 \le j_f \le 14$. (The highest energetically allowed rotational state is $j_f = 16$.) Predictions of the cross sections on the basis of two different potential surfaces (described below) also appear in that figure. The experiment does not determine absolute differential cross sections, and in each panel, the experimental data have been scaled to match the average integral cross section calculated from the two theoretical results. A table of the experimental values shown in Figure 3 is available as Supporting Information.

6. Calculations

Differential cross sections for Ne−CO scattering were computed for two ab initio potentials: the symmetry adapted perturbation theory surface[1] of Moszynski et al. and the CCSD-(T) surface S2 of McBane and Cybulski.[3] The calculations were carried out with the MOLSCAT program[34] using the hybrid Airy/log-derivative propagator of Alexander and Manolopolous.[35] Full close-coupled calculations were performed. Details of the computations were described earlier.[3]

The calculated differential cross sections were averaged with three-point Gauss-Hermite quadrature over a Gaussian collision energy distribution centered at 511 cm^{-1} with a 25 cm^{-1} standard deviation. In addition, contributions from two initial rotational states of CO, $j = 0$ and 1, were added with weights 0.77 and 0.23 to reflect the initial rotational distribution in the molecular beam.

7. Discussion

7.1. Errors in Experiment and Analysis. No error bars appear in Figure 3. We omit them because some systematic deviations remain between the raw data and our simulated images, so statistically estimated error bars may not be meaningful. We can, however, give a qualitative discussion of likely errors.

For most final j levels, we collected two independent data sets many months apart. The results presented here come largely from the second set, which has better signal-to-noise ratios and better velocity mapping. However, the image features and the extracted differential cross sections from the two sets are nearly identical; no qualitative differences, and only minor ($\le$10%) quantitative differences, appear between the two sets. We conclude that the experimental conditions and procedures are

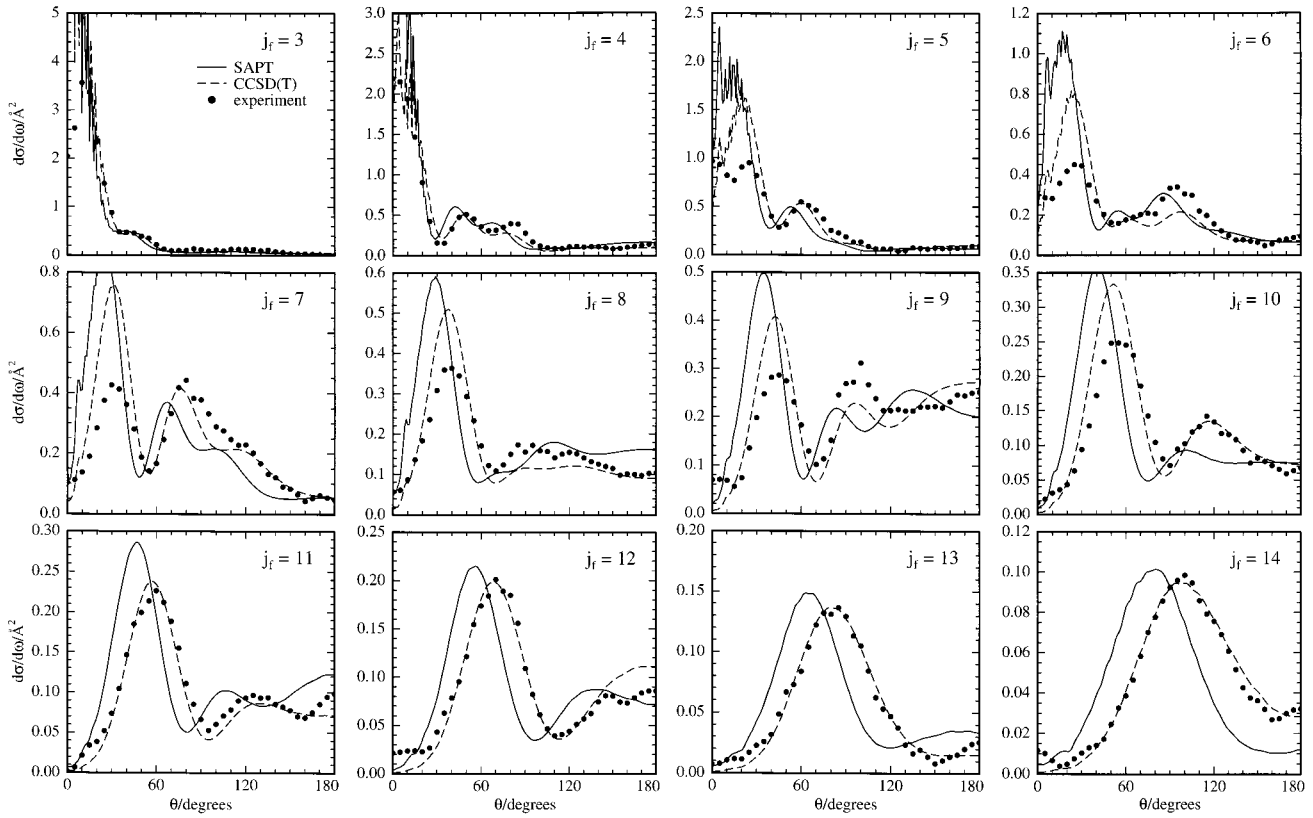

Figure 3. Experimental and calculated state-to-state differential cross sections.

reproducible and reliable. Most of the uncertainty in the results therefore comes from uncertainty in the model of the experiment used in extracting differential cross sections from the image data.

The characteristics of the experiment that contribute the most to the uncertainty are the properties of the ion optics, the polarization dependence of the ionization probability, and the location of the laser focus. The position and orientation of the detector, the speed ratios of the molecular beams, and the center frequency of the laser with respect to the absorption frequency of a stationary CO molecule also affect the results, but they are well constrained by the data. Other characteristics of the simulation program, including the radial distributions of molecular beam density, the temporal lengths of the molecular beam pulses, and the shape of the laser beam, have much weaker effects on the extracted differential cross sections.

In the experiment, the laser beam is nearly perpendicular to the relative velocity vector. That geometry reduces the impact of displacement of the laser focus along the propagation direction. Such displacements enhance the intensity near the "top" of the image (near the zero lab frame velocity point) and in a broad band near the "bottom", where molecules moving along the laser propagation direction appear. The enhanced regions correspond to scattering angles near 90° in the present experiment. An unintended 1.5 mm displacement of the laser focus from the molecular beam crossing region has the effect of artificially inflating the amplitude of peaks near 90° by about 30%. However, it has almost no effect on the positions of the extracted maxima. The largest disagreements between the extracted DCSs and the calculated ones are in the relative heights of DCS maxima in forward and sideways scattering regions. It is possible that such an unintended displacement contributes to that disagreement.

To check for the possibility that errors in the model or in the placement of the laser focus along the propagation direction were distorting the results, a second set of analyses was carried out in which the bright region near the top of the image was ignored and the DCS was determined only from the lower, more uniform part. The results from these fits were the same as those from the ones that used all of the data.

Side-to-side displacements of the laser focus can enhance the forward scattered part of the image with respect to the backscattered part or vice versa. During the experiments we chose a laser position that produced symmetric images when both molecular beams contained the same CO/Ar sample and the ion optics were defocused to produce an image dependent on both position and velocity of the ions. This procedure ensures that the side-to-side laser displacement error is small compared to the size of the molecular beams at the intersection region and should reduce forward−backward bias in the detection.

The speed distributions in the molecular beams spread out the parts of the image corresponding to fast-moving molecules (in our geometry, the bottom of the image) more than the parts corresponding to slow molecules. This property of the images is accurately modeled in the fitting procedure.

The laser light was polarized in the plane of the two molecular beams. The transition used in the REMPI probe is sensitive to alignment of the angular momentum vectors of the molecules. If the molecules appearing in any particular pixel of the image have a nonzero laboratory frame alignment, systematic errors in the pixel intensities might appear. We have tested the importance of this effect by performing several fits of the same image with different assumptions about the alignment of the molecules. Those tests show that for our geometry and probe transition the extracted intensities of well-resolved features in the differential cross section can change by at most a factor of

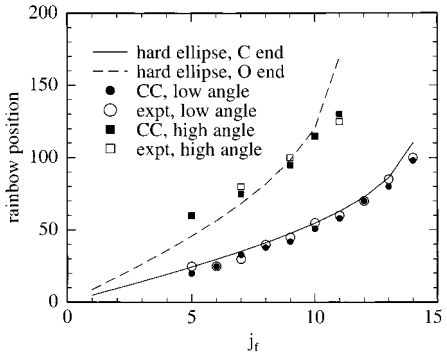

Figure 4. Expected locations of classical hard-ellipse rotational rainbows compared to CC calculations (on the CCSD(T) surface) and experimental results.

2 when the alignment goes from one extreme to the other. The actual alignment expected in our experiment is much smaller. Even in the extreme case, however, the positions of maxima in the DCS are affected very little.

Finally, the data do not determine the differential cross section with equal uncertainty at every scattering angle. At very small angles, high-j population in the unscattered beam can obscure the scattered signal. Regions of the image that are "contaminated" in this way were not included in the computation of χ^2. In addition, the image-space basis functions at scattering angles near 0 and π are more nearly linearly dependent than those at intermediate deflections. The regularization procedure introduces a bias toward a constant differential cross section, and this bias is important in regions where the data do not constrain the DCS well. In our results, the bias is important only near scattering angles of 0 and π. Cross sections that appear nearly flat in those regions may not be tightly constrained by the data.

We conclude that our extracted differential cross sections represent the positions of well resolved features with angular accuracy of 2° or better. The relative amplitudes of maxima in different parts of the DCS are more uncertain; the combined uncertainties from laser positioning and polarization effects could produce an error on the order of 40% in amplitude ratios between different peaks.

7.2. Interpretation of Observed Structures. The observed differential cross sections display several maxima that move gradually to higher scattering angle as j_f increases. In this section, we attempt to assign these maxima to particular physical origins.

A prominent maximum appears near zero scattering angle in the $j_f = 3$ cross section and moves steadily outward, appearing near 35° at $j_f = 7$ and 55° at $j_f = 10$ and finally becoming the only clear maximum at $j_f = 13$ at a scattering angle near 90°. We assign this maximum to a rotational rainbow corresponding to scattering from the carbon end of the molecule, on the basis of the classical hard ellipse model of Bosanac and Buck.[36] For this calculation, hard ellipse parameters estimated from the 460 cm^{-1} contour of the McBane and Cybulski Ne−CO potential surface[3] were used. The semimajor and semiminor axes of the ellipse were $A = 3.16$ Å and $B = 2.61$ Å, respectively. The shift δ of the center of mass from the center of symmetry was 0.22 Å, and the parameter $\epsilon = \mu/I$ was 1.28 $Å^{-2}$.

Figure 4 shows the positions of the observed maxima and the positions of the carbon-end rainbow obtained from the hard ellipse model. The low angle maxima follow the predicted curve remarkably closely. The filled circles give the positions of the corresponding maxima in the differential cross sections computed by close-coupling methods on the McBane and Cybulski surface. These agree well both with the hard ellipse model and with the experimental results.

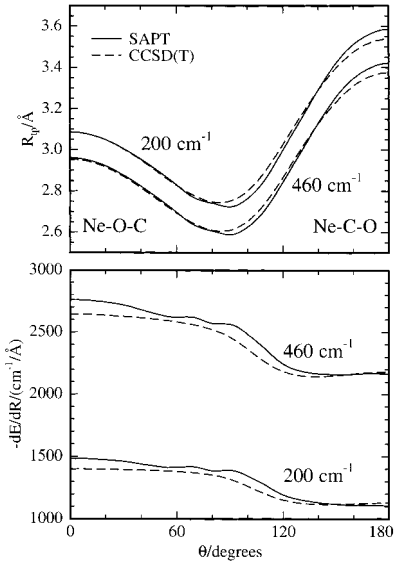

Figure 5. Upper panel: potential contours in the repulsive region for the two surfaces. Lower panel: radial steepness ($-dE/dR$) along the same contours for the two surfaces.

The situation at higher scattering angles is murkier. In that region, we expect to observe both supernumary rainbows connected with the C-end rainbow and a second classical rainbow from scattering at the oxygen end of the molecule.[37] These two routes to the same outcome can interfere, producing a complicated pattern in the differential cross section. The interference is the source of the oscillations in integral cross sections as a function of j_f reported previously.[3] In the experimental data, clear maxima appear at high scattering angles in some of the results, whereas in others, the pattern is more complicated. Figure 4 shows the observed and calculated (by CC calculations on the McBane and Cybulski surface) maximum positions and their expected positions on the basis of the hard ellipse model. It is not clear that even these relatively isolated maxima correspond to the O-end rainbow. We conclude that, although the strong maximum at low scattering angles does correspond to the C-end rainbow, the differential cross section at higher angles will be influenced by collisions at both ends of the molecule.

7.3. Comparisons with Computed Cross Sections. The qualitative shapes of the calculated cross sections, and the trends in them with increasing Δj, agree remarkably well with the experimental results. Most of the cross sections show two or three maxima, and these appear in the experimental results and both theoretical curves. The differences take two forms: disagreements about the angular positions of the maxima and disagreements about the relative intensities of different maxima.

The prominent C-end rotational rainbow peak is the lowest angle and highest intensity maximum in both theoretical cross sections and in the experimental results for most values of Δj. The position of this peak is predicted accurately in nearly every case by the CCSD(T) surface. The SAPT surface, on the other hand, usually underestimates the scattering angle for this maximum. The difference first appears clearly at $\Delta j = 6$ and continues throughout the series.

The difference between the two predictions is consistent with the different anisotropies. The upper panel of Figure 5 shows the 200 and 460 cm^{-1} contours of both surfaces. The SAPT surface is thinner and more elongated, so a lower scattering angle

is sufficient to produce a given Δj. The classical hard ellipse model with ellipse axis lengths taken from the SAPT 460 cm^{-1} contour predicts a $\Delta j = 10$ C-end rainbow peak shifted to lower scattering angle from the CCSD(T) one by 6−7°. The CC calculation, however, shows a 12° shift. The small difference in anisotropy at the classical turning point contour explains only about half the observed shift in rainbow positions.

The lower panel of Figure 5 shows the steepnesses of the two surfaces along the 200 and 460 cm^{-1} contours. Differences in the steepness imply different amounts of impulsive character of the collisions and might contribute to the different predicted rainbow positions. The steepnesses ($-dE/dR$) are very similar at the carbon end, but the SAPT potential is steeper than the CCSD(T) one at any approach more than about 45° from the C end of CO. The greater steepness of the SAPT surface in the region $90° \leq \theta \leq 130°$ probably does contribute to the additional shift in the predicted C-end rainbow position.

At higher scattering angle, the CCSD(T) surface continues to describe the locations of DCS maxima accurately. Maxima in the SAPT predicted DCS generally appear about 20° to lower scattering angle. The substantially different steepnesses of the two surfaces near the O end of CO and the different supernumary rainbows expected from the C-end scattering probably both contribute to the different predictions for the DCS at high scattering angles.

The experimental results show a larger amount of sideways and backward scattering than the predictions. A discussion of the possible errors in our extractions of these relative amplitudes from the raw data appeared above. The level of disagreement between experiment and theory on this point is larger than we feel can be attributed solely to errors in the experiment and analysis.

We conclude that the SAPT repulsive wall is too anisotropic. The CCSD(T) surface, although it does not describe the van der Waals well as accurately as the SAPT potential, does a better job of describing the shape of the repulsive wall. The difference is particularly clear for scattering at the C end of CO, because scattering there is the only contributor to the low angle part of the DCS. At higher scattering angles, the data reflect properties of the entire potential surface. These data support and clarify the conclusions reached by Antonova et al.[17] and McBane and Cybulski[3] on the basis of integral cross section measurements.

Acknowledgment. We acknowledge Mark Jaska for his expert technical help. G.C.M. is grateful for helpful suggestions from Gregory Hall and Giacinto Scoles and an analytical Jacobian program from Mike Westley. Computations were performed at the Ohio Supercomputer Center. This work is supported by the U.S. Department of Energy, Office of Basic Energy Sciences, Division of Chemical Sciences.

Supporting Information Available: A table showing all of the experimentally determined relative differential cross sections displayed in Figure 3. This material is available free of charge via the Internet at http://pubs.acs.org.

References and Notes

(1) Moszynski, R.; Korona, T.; Wormer, P. E. S.; van der Avoird, A. *J. Phys. Chem. A* **1997**, *101*, 4690−4698.

(2) Jeziorski, B.; Moszynski, R.; Szalewicz, K. *Chem. Rev.* **1994**, *94*, 1887−1930.

(3) McBane, G. C.; Cybulski, S. M. *J. Chem. Phys.* **1999**, *110*, 11734−11741.

(4) Subramanian, V.; Chitra, K.; Sivanesan, D.; Amutha, R.; Sankar, S. *Chem. Phys. Lett.* **1999**, *307*, 493−496.

(5) Kestin, J.; Ro, S. T.; Wakeham, W. A. *Ber. Bunsen-Ges. Phys. Chem.* **1982**, *86*, 753−760.

(6) Trengrove, R. D.; Robjohns, H. L.; Dunlop, P. J. *Ber. Bunsen-Ges. Phys. Chem.* **1984**, *88*, 450−453.

(7) Imaishi, N.; Kestin, J. *Phys. A* **1984**, *126*, 98−115.

(8) Brewer, J. *AFOSR Technical Report MRL-2915-C*; 1967, cited in Ref 9. Available from NTIS, 5285 Port Royal Rd., Springfield, VA, 22161 as document AD663448.

(9) Moszynski, R.; Korona, T.; Heijmen, T. G. A.; Wormer, P. E. S.; van der Avoird, A.; Schramm, B. *Polish J. Chem.* **1998**, *72*, 1479.

(10) Vatter, K.; Schmidt, H. J.; Elias, E.; Schramm, B. *Ber. Bunsen-Ges. Phys. Chem.* **1996**, *100*, 73−79.

(11) Nerf, R. B. Jr.; Sonnenberg, M. A. *J. Mol. Spectrosc.* **1975**, *58*, 474−478.

(12) Henry, A.; Hurtmans, D.; Margottin-Maclou, M.; Valentin, A. *J. Quantum Spectrosc. Rad. Transfer* **1996**, *56*, 647−671.

(13) Randall, R. W.; Cliffe, A. J.; Howard, B. J.; McKellar, A. R. W. *Mol. Phys.* **1993**, *79*, 1113−1126.

(14) McKellar, A. R. W.; Chan, M. C. *Mol. Phys.* **1998**, *93*, 253−262.

(15) Walker, K. A.; Ogata, T.; Jäger, W.; Gerry, M. C. L.; Ozier, I. *J. Chem. Phys.* **1997**, *106*, 7519−7530.

(16) Winnewisser, G.; Dumesh, B. S.; Pak, I.; Surin, L.; Lewen, F.; Roth, D. A.; Rusin, F. S. *J. Mol. Spectrosc.* **1998**, *192*, 243−246.

(17) Antonova, S.; Lin, A.; Tsakotellis, A. P.; McBane, G. C. *J. Chem. Phys.* **1999**, *110*, 11742−11748.

(18) Eppink, A. T. J. B.; Parker, D. H. *Rev. Sci. Instrum.* **1997**, *68*, 3477−3484.

(19) Scoles, G., Ed.; *Atomic and Molecular Beam Methods*; Oxford University Press: New York, 1988.

(20) Bontuyan, L. S.; Suits, A. G.; Houston, P. L.; Whitaker, B. J. *J. Phys. Chem.* **1993**, *97*, 6342−6350.

(21) Kitsopoulos, T. N.; Buntine, M. A.; Baldwin, D. P.; Zare, R. N.; Chandler, D. W. *Science* **1993**, *260*, 1605−1610.

(22) Yonekura, N.; Gebauer, C.; Kohguchi, H.; Suzuki, T. *Rev. Sci. Instrum.* **1999**, *70*, 3265−3270.

(23) Ahmed, M.; Peterka, D. S.; Suits, A. G. *Chem. Phys. Lett.* **1999**, *301*, 372−378.

(24) Ahmed, M.; Peterka, D.; Suits, A. *Chem. Phys. Lett.* **2000**, *317*, 264−268.

(25) Ahmed, M.; Peterka, D. S.; Suits, A. G. *Phys. Chem. Chem. Phys.* **2000**, *2*, 861−868.

(26) Lorenz, K. T.; Westley, M. S.; Chandler, D. W. *Phys. Chem. Chem. Phys.* **2000**, *2*, 481−494.

(27) Westley, M. S.; Lorenz, K. T.; Chandler, D. W.; Houston, P. L. *J. Chem. Phys.* **2001**, *114*, 2669−2680.

(28) Proch, D.; Trickl, T. *Rev. Sci. Inst.* **1989**, *60*, 713−716.

(29) Hines, M. A.; Michelsen, H. A.; Zare, R. N. *J. Chem. Phys.* **1990**, *93*, 8557−8564.

(30) Heck, A. J. R.; Chandler, D. W. *Annu. Rev. Phys. Chem.* **1995**, *46*, 335−372.

(31) Winterhalter, J.; Maier, D.; Honerkamp, J.; Schyja, V.; Helm, H. *J. Chem. Phys.* **1999**, *110*, 11187−11196.

(32) McBane, G. C. Simulation and Analysis of Image Data from Crossed Beam Experiments. In *Imaging in Chemical Dynamics*; Suits, A. G., Continetti, R. E., Eds.; ACS Books: Washington, DC, 2000.

(33) Press, W. H.; Teukolsky, S. A.; Vetterling, W. T.; Flannery, B. P. *Numerical Recipes in C: the Art of Scientific Computing*, 2nd ed.; Cambridge University Press: New York, 1992.

(34) Hutson, J. M.; Green, S. *MOLSCAT computer code*, version 14; distributed by Collaborative Computational Project No. 6 of the Engineering and Physical Sciences Research Council, UK, 1994.

(35) Alexander, M. H.; Manolopoulos, D. E. *J. Chem. Phys.* **1987**, *86*, 2044−2050.

(36) Bosanac, S.; Buck, U. *Chem. Phys. Lett.* **1981**, *81*, 315−19.

(37) Korsch, H. J.; Schinke, R. *J. Chem. Phys.* **1980**, *73*, 1222−1232.